Bioorganic activated carbon from cashew nut shells for H$_2$ adsorption and H$_2$/CO$_2$,

(article starts on next page)

Bioorganic activated carbon from cashew nut shells for H₂ adsorption and H₂/CO₂, H₂/CH₄, CO₂/CH₄, H₂/CO₂/CH₄ selectivity in industrial applications

Jarosław Serafin [a,*], Bartosz Dziejarski [b,c], Óscar Javier Fonseca-Bermúdez [d], Liliana Giraldo [e], Rocío Sierra-Ramírez [d], Marta Gil Bonillo [a], Ghulam Farid [f,g], Juan Carlos Moreno-Piraján [h,**]

[a] *Department of Inorganic and Organic Chemistry, Inorganic Chemistry Section, University of Barcelona, Martí i Franquès 1-11, 08028, Barcelona, Spain*
[b] *Department of Space, Earth and Environment, Division of Energy Technology, Chalmers University of Technology, SE-412 96, Gothenburg, Sweden*
[c] *Faculty of Environmental Engineering, Wroclaw University of Science and Technology, 50-370, Wroclaw, Poland*
[d] *Department of Chemical and Food Engineering, Universidad de Los Andes, 111711, Bogotá, Colombia*
[e] *Departamento de Química, Universidad Nacional de Colombia, 111711, Bogotá, Colombia*
[f] *Department of Applied Physics, University of Barcelona, C/Martí i Franquès, 1, 08028, Barcelona, Catalunya, Spain*
[g] *ENPHOCAMAT Group, Institute of Nanoscience and Nanotechnology (IN2UB), University of Barcelona, C/ Martí i Franquès, 1, 08028, Barcelona, Catalunya, Spain*
[h] *Departamento de Química, Grupo de Investigación en Sólidos Porosos y Calorimetrái, Universidad de Los Andes, 111711, Bogotá, Colombia*

ARTICLE INFO

ABSTRACT

This research explores the production of activated carbon (AC) from cashew nut shells using a potassium hydroxide (KOH) activation method, with a focus on its application in high-pressure gas adsorption. Among the synthesized samples, AC850 demonstrated the highest efficiency, displaying a specific surface area of 1972 m²/g and total and micropore volumes of 0.847 cm³/g and 0.724 cm³/g, respectively. The bioorganic activated carbon exhibited significant sorption capabilities for H₂, with uptake values of 13.34 mmol/g (2.69 wt%) at 10 bar and 25 °C, and a H₂/CH₄ selectivity range between 43.4 and 2.6. Calculations were also conducted for selectivity in a mixture of three gases (H₂, CO₂, and CH₄) in industrial settings. Advanced characterization methods such as N₂/CO₂ adsorption isotherms, FT-IR, Raman spectroscopy, SEM, and TGA were employed to analyze the structural and chemical properties of the produced AC, including its functional groups and molecular structure. The research underscores the potential of utilizing agricultural waste, particularly cashew nut shells, to develop efficient materials for H₂ storage and purification. The high-pressure adsorption capability and eco-friendly nature of the manufactured activated carbon make it suitable for both environmental and industrial applications.

1. Introduction

The shift towards a hydrogen-based economy has become increasingly evident in recent years. Historically, hydrogen production was dominated by methods such as steam methane reforming (SMR) and coal gasification, which significantly depend on fossil fuels and contribute to greenhouse gas emissions. Currently, there's a marked shift towards more sustainable production techniques, with a particular focus on electrolysis driven by renewable energy sources. The primary benefit of this approach is its environmental friendliness, producing only water and heat without CO₂ emissions, thereby decreasing greenhouse gases and alleviating air pollution. Moreover, hydrogen can be

sustainably regenerated through direct electrolysis of water using renewable energy sources, creating a sustainable cycle [1]. The quest for efficient gas separation technologies underpins the pivotal challenges faced by various industries, ranging from energy production to environmental protection. Gas separation plays a crucial role in numerous industrial processes, significantly impacting environmental sustainability. Gas separation processes, essential in the chemical and petrochemical sectors, account for a substantial portion of the operational and capital expenditures due to their energy-intensive nature. The increasing awareness of sustainable development has propelled the search for innovative processes that enhance material and energy efficiency, thereby reducing costs, energy consumption, and waste generation. Gas

---

* Corresponding author.
** Corresponding author.

E-mail addresses: jaroslaw.serafin@qi.ub.es (J. Serafin), jumoreno@uniandes.edu.co (J.C. Moreno-Piraján).

separation technologies, notably adsorption, are at the forefront of this quest, offering opportunities for significant improvements in efficiency and applicability. Innovations in adsorbent materials, coupled with advancements in process development and optimization, are crucial for expanding the scope and enhancing gas separation efficiency by adsorption.

Industries utilize a myriad of gases, including CO_2 and H_2, which serve critical roles in various applications such as energy storage, environmental management, and manufacturing processes. Efficient separation and storage of these gases are vital for operational efficiency and environmental stewardship. The challenge lies in developing gas separation solutions that are not only effective but also environmentally sustainable and economically viable. Multiple methods exist for hydrogen storage, encompassing high-pressure compressed gas, cryogenic liquids in dedicated tanks, and hydride formation [2]. Each method offers unique benefits and drawbacks, making the choice of storage solution context-dependent. Hydrogen carriers, such as ammonia (NH_3), along with solid materials, are pivotal in this area [3]. A particularly promising hydrogen storage approach that has attracted significant attention is based on adsorption [4]. Key to this strategy is understanding how hydrogen interacts with solid surfaces. Various solid adsorbents are being explored for hydrogen storage, including metal-organic frameworks (MOFs), zeolites, and carbon-based substances [5].

Among them, activated carbon derived from biomass, emerges as a sustainable and efficient adsorbent for H_2 storage. Its unique properties, such as high surface area, porosity, and tunable surface chemistry, make it an ideal candidate for adsorption processes. Biomass-derived activated carbon, in particular, offers a greener alternative to traditional adsorbents, providing an opportunity to leverage waste materials for environmental and energy applications. Activated carbons, known for their porous nature and versatile adsorption capabilities, play a significant role in H_2 adsorption due to their textural characteristics, high surface area, tunable porosity, high degree of surface reactivity, good stability, and affordable low price for industrial applications [6,7]. Globally, the annual production of activated carbon is estimated to reach approximately 100,000 tons [8]. Predominant sources for commercial-scale activated carbon include wood, anthracite, bitumen charcoal, lignite, peat shell, and coconut. Additionally, alternative sources like olive and almond shells are increasingly being utilized. The carbon content of these materials varies from 40 to 90% (wt.), with a density ranging from 0.4 to 1.45 g/m^3 [9–12]. Efforts have been directed towards leveraging waste as raw materials for activated carbon production [13]. Agricultural residues, such as olive cores, biomass, rice husks, corn stalks, bagasse, fruit Stones (cherry and apricot stones, grape seeds), hard shell (pistachio, almond, and pecant shells), fruit pulp, bones, and coffee beans, can also serve as sources [14]. The chosen raw material for activated carbon preparation should ideally be abundant, cost-effective, and safe [15]. Furthermore, minimizing mineral content and ensuring minimal biodegradability during initial storage are crucial considerations [16]. This approach aligns with the principles of sustainable development, offering a pathway to reduce environmental impact while addressing the critical need for efficient gas separation.

The use of activated carbon in capturing and separating H_2 gas demonstrates its versatility and effectiveness. Its application spans various domains, from enhancing energy efficiency in natural gas processing to mitigating greenhouse gas emissions. The potential of activated carbon to selectively adsorb and separate these gases underscores its significance in addressing the challenges of modern industrial processes.

This study presents a novel approach to address both waste management challenges and the development of sustainable gas adsorption technologies. Our work focuses on the synthesis and application of activated carbons derived from cashew nut shells, utilizing a potassium hydroxide activation method. The utilization of agricultural waste as a precursor for AC production represents a solution to the growing problem of waste accumulation while offering a sustainable pathway for resource utilization. The key novelty of this research lies in the integration of waste management principles with the exploration of high-pressure gas adsorption capabilities of the synthesized activated carbons. By repurposing cashew nut shells, an abundant agricultural by-product, not only mitigate environmental concerns associated with waste disposal but also unlock the potential for value-added materials with diverse applications. Through comprehensive characterization utilizing advanced analytical techniques such as N_2/CO_2 adsorption isotherms, Fourier-transform infrared spectroscopy (FT-IR), Raman spectroscopy, scanning electron microscopy (SEM), and thermogravimetric analysis (TGA), we provide detailed insights into the structural, chemical, thermal, and morphological properties of the synthesized activated carbons. Furthermore, this research emphasizes the practical significance of activated carbon derived from agricultural waste in the realm of gas adsorption, particularly focusing on H_2 storage and purification. By exploring the adsorption capabilities of ACs under high-pressure conditions, we contribute to the development of efficient and environmentally friendly materials for gas separation and purification processes.

2. Methodology

2.1. Preparation of activated carbons

Activated carbon preparation from biochar involved several steps to achieve the desired properties, as shown in Fig. 1. Initially, cashew nut shells (CNS) were finely ground until the entire sample passed through a 4 mm screen. To prevent decomposition of components or microbial proliferation, the ground CNS was stored at $-4\ °C$. Subsequently, the 50 g of CNS was placed in the hot zone of a tube furnace, and heating was initiated with a ramp rate of 5 °C/min until reaching a final temperature of 550 °C. This temperature was determined based on prior experiments aimed at producing biochar devoid of CNSL remnants. Pyrolysis was maintained for 3 h under a nitrogen flux of 150 mL/min, resulting in the production of 8.66 ± 1.35 g of biochar.

Following biochar production, chemical activation was conducted using potassium hydroxide (KOH) according to the methodology outlined by Cruz-Reina et al. [17]. The biochar was impregnated with solid KOH at a mass ratio of 1:1 (char) and allowed to react under agitation at 150 rpm for 3 h at 80 °C. Subsequently, the solution was oven-dried at 120 °C overnight. The impregnated samples were then subjected to activation in a tube furnace at temperatures of 800 °C, 850 °C, and 900 °C (designated as AC800, AC850, and AC900) for 3 h under a nitrogen atmosphere with a flux of 50 mL/min and a heating rate of 5 °C/min.

Multiple reactions have been proposed to explain the activation process during the thermal treatment, but in the most broadly accepted KOH reacts with the carbonous precursor forming potassium carbonate, potassium oxide and metallic potassium, which are eliminated during the hot water rinsing. At high temperatures, biomass decomposes into gaseous, liquid, and solid products. In the presence of KOH, the pyrolysis process is catalyzed, facilitating the formation of gaseous hydrocarbons such as propane (C_3H_8) and propene (C_3H_6) through decarboxylation (removal of carboxyl groups) and dehydration (removal of water) mechanisms. Furthermore, KOH reacts with the volatile products of pyrolysis, contributing to the formation of hydrocarbons and inorganic products such as potassium carbonate (K_2CO_3) and potassium oxide (K_2O). The resulting hydrogen (H_2) is also one of the main gaseous products, as shown on the below equations [18–20].

- In this reaction, KOH reacts with carbon (C) to form potassium carbonate (K_2CO_3), metallic potassium (K), and hydrogen gas (H_2). This reaction suggests that KOH serves as both a chemical reagent and an activating agent, creating pores in the carbon structure.
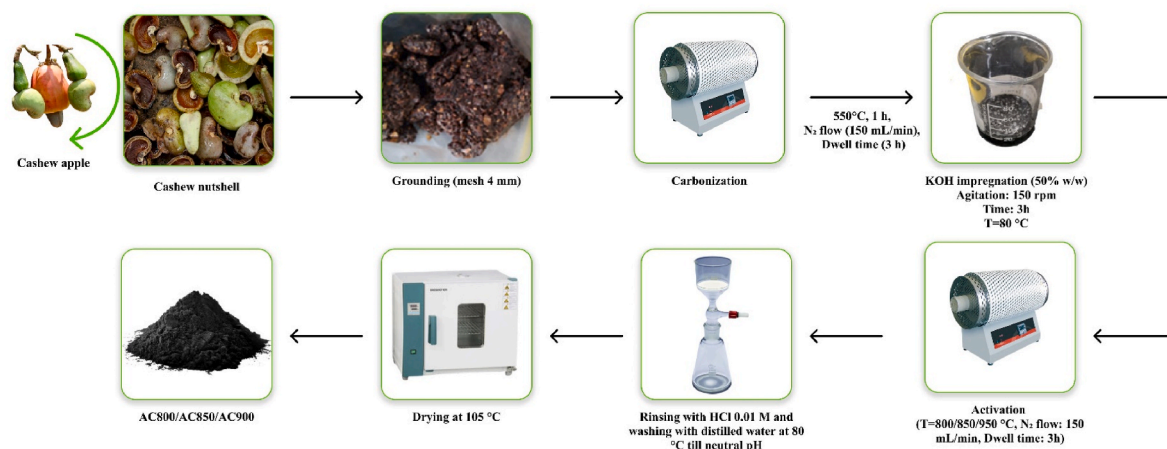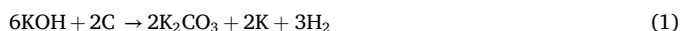
Fig. 1. Schematic preparation of activated carbon derived from cashew nut shells.

$$6KOH + 2C \rightarrow 2K_2CO_3 + 2K + 3H_2 \tag{1}$$

●Here, KOH reacts with a hydrocarbon such as propylene (C_3H_6) to produce potassium carbonate (K_2CO_3), potassium oxide (K_2O), and hydrogen gas (H_2). This reaction indicates that KOH not only reacts with pure carbon but also with more complex carbon-containing compounds.

$$8KOH + 2C_3H_6 \rightarrow 2K_2CO_3 + 2K_2O + 5H_2 \tag{2}$$
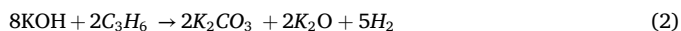
●In this reaction, KOH interacts with propane (C_3H_8) to yield potassium carbonate (K_2CO_3), potassium oxide (K_2O), and hydrogen gas (H_2). This demonstrates the versatility of KOH in reacting with various carbon-based materials.

$$4KOH + 2C_3H_8 \rightarrow K_2CO_3 + K_2O + 3H_2 \tag{3}$$
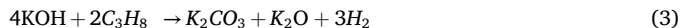
After the activation process, the resulting potassium compounds (K_2CO_3, K_2O, and metallic K) need to be removed. This is usually done through water rinsing, which dissolves these compounds, leaving behind a highly porous and activated carbon structure. The elimination of these compounds is crucial for achieving high surface area and desired porosity in the final activated carbon product.

2.2. Characterization of carbon-based materials

TGA analysis is used to measure the weight loss and thermal reactions of the CNS during pyrolysis in an inert environment. 10–20 mg of the sample is heated at a rate of 10 °C/min until it reaches a temperature of 900 °C. The heating procedure is carried out with a nitrogen flow rate of 100 mL/min utilizing a STA 7200 Hitachi High-Tech equipment that has the TAT 81 7200 standard analysis software. Activated carbon's structure is analyzed by scanning electron microscopy (SEM) with the JSM 6490-LV JEOL instrument. FT-IR spectroscopy is used to detect functional groups in the activated carbon. The Thermo Scientific Nicolet 6700 equipment is used to scan within the 400-4000 cm^{-1} range. The sample is manufactured by combining KBr to make a tablet with a solid-KBr ratio of 0.1%. Raman spectroscopy is conducted using the Xplora model dispersive Raman spectrometer by Horiba Scientific. The device has a confocal microscope and three laser excitation lines with wavelengths of 514 nm, 632 nm, and 785 nm. The Raman spectra are detected using a CCD detector. XRD.

Nitrogen adsorption-desorption isotherms are performed at a temperature of −196 °C to analyze the textural features of the materials studied in this research. Approximately 0.1 g of carbonaceous materials undergo degassing at 250 °C for many hours utilizing a Micromeritics ASAP 2020 apparatus. The BET technique is used to determine the specific surface area. The Dubinin-Astakhov technique is used to evaluate the volume of micropores. The pore size distribution is determined using the NLDFT model. Micropore volumes (<1.4 nm) and narrow micropore volumes (<0.7 nm) were determined by measuring CO_2 (99.99% pure) adsorption at 0 °C.

High-pressure adsorption isotherms were conducted using Micromeritics' ASAP 2050 sorption analyzer, which is intended to achieve pressures above 15 bar. Hydrogen adsorption was conducted at 0 and 25 °C up to 10 bars, and high-pressure adsorption isotherms of CO_2 and CH_4 were measured up to 10 bars at a temperature of 25 °C.

Six isotherm models were used to analyze the experimental H_2 data, including two-parameter models (Langmuir, Freundlich, Temkin) and three-parameter models (Redlich–Peterson, Toth, and Sips). The isotherm assumptions provide a description of the adsorption phenomena and the equations for several models are shown in Table 1. Moreover, non-linear regression analysis was conducted using the Solver Add-In in Microsoft Excel to accurately model the specified isotherm equations to empirical adsorption equilibrium observations. This enabled the derivation of a precise isotherm equation by identifying the optimal parameter values to match the data. We assessed the fitting quality in isotherm modeling by calculating the sum of squares error (SSE), where a lower SSE value signifies a better fit. The SSE is determined by adding up the squares of the discrepancies between the actual data points and the estimated values of the dependent variable derived from the model. The SSE is calculated using the formula:

$$SSE = \sum_{i=1}^{n} \left(q_{e,observed} - q_{e,predicted} \right)^2 \tag{4}$$

Where: qe, observed represents the experimental quantities of H_2 adsorbed at equilibrium in mmol/g, whereas qe, predicted indicates the theoretical amounts determined from a certain isotherm model in mmol/g.

3. Results and discussion

3.1. Textural properties

The porous structure of activated carbons derived from cashew nut shells was investigated through nitrogen physical adsorption. Fig. 2 depicts the nitrogen adsorption-desorption isotherms for activated carbons prepared at varying activation temperatures. Notably, all activated carbons exhibited a rapid increase in nitrogen adsorption capacity at low relative pressures ($P/P^0 < 0.1$), indicating the presence of abundant micropores within the porous carbon structure. Moreover, the isotherms demonstrated an augmentation in adsorption capacity with increasing temperature at low relative pressures, with AC850 showcasing the

Table 1
Description of selected adsorption isotherm models.

| Isotherm model	Described adsorption phenomenon	Non-linear model equations	Parameters of the equation	Reference
Langmuir	Monolayer adsorption on homogeneous surface	$q_e = q_m \frac{K_L \bullet P}{(1 + K_L \bullet P)}$	q_e - experimental amount of adsorbed adsorbate [mmol/g], q_m - maximum adsorption capacity (mmol/g), P - relative pressure of the adsorbate (bar), K_L - Langmuir isotherm constant (bar^{-1})	[21]
Freundlich	Multilayer adsorption on heterogeneous surface	$q_e = K_F \bullet P^{\frac{1}{n_F}}$	K_F - Freundlich isotherm constant (bar^{-1}), $1/n_F$ – heterogeneity factor, n_F – Freundlich exponent (−)	[22]
Redlich–Peterson	Includes the features of both Langmuir and Freundlich isotherm	$q_e = \frac{K_{RP} \bullet P}{1 + a_{RP} \cdot P^{\beta_{RP}}}$	K_{RP} - Redlich-Peterson isotherm constant (bar^{-1}), a_{RP} - Redlich-Peterson model constant (bar^{-1}), β_{RP} – exponent (−)	[23]
Toth	Adsorption on heterogeneous surfaces	$q_e = \frac{q_m \bullet K_T \bullet P}{[1 + (K_T \bullet P)^{n_T}]^{\frac{1}{n_T}}}$	q_m - maximum adsorption capacity (mmol/g), K_T - Toth isotherm constant (bar^{-1}), n_T – heterogeneity factor (−)	[24]
Sips	Combined form of the Langmuir and Freundlich model equations to characterize heterogenous adsorption systems	$q_e = \frac{q_m \bullet (K_S \bullet P)^{\frac{1}{n_S}}}{1 + (K_S \bullet P)^{\frac{1}{n_S}}}$	q_m - maximum adsorption capacity (mmol/g), K_S - Sips isotherm constant (bar^{-1}), n_S – Sips isotherm exponent (−)	[25]
Temkin	Adsorption occurring on heterogeneous surfaces with a nonuniform energy distribution	$q_e = B \bullet \ln(K_T \bullet P)$	B -Temkin constant (−), K_T - adsorption equilibrium constant (bar^{-1})	[26]
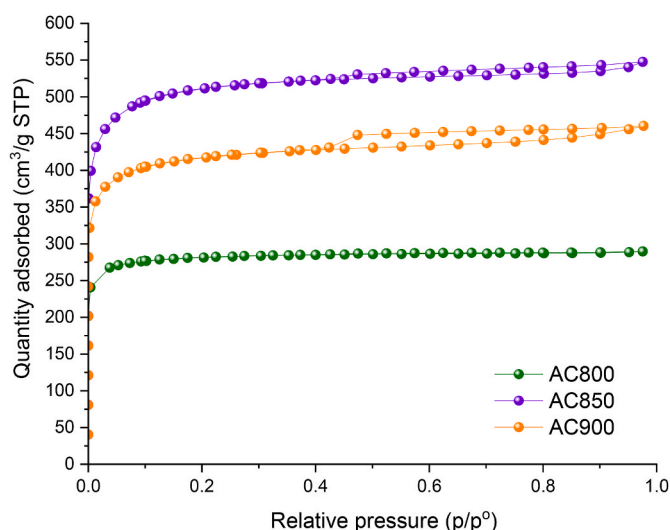
Fig. 2. N_2 adsorption-desorption isotherms of activated carbons.

highest adsorption capacity at 850 °C. Elevated calcination temperatures up to 850 °C contributed to a heightened degree of graphitization in activated carbons, thereby bolstering their structural stability and augmenting adsorption capacity. However, exceeding this temperature threshold may lead to the detrimental breakdown of micropores and the formation of larger pores. This phenomenon, termed "pore coalescence," can diminish the specific surface area and porosity of the material [27]. Hence, the optimal calcination temperature range for achieving the desired level of graphitization while preserving pore structure integrity ideally falls within 800–850 °C. According to the established IUPAC classification, the adsorption-desorption isotherms obtained from the activated carbons displayed a distinctive blend of characteristics resembling both type I and type IV isotherms. Type I isotherms, which are typically associated with microporous materials, signify a rapid increase in adsorption at low relative pressures (P/P0 < 0.1), suggesting the presence of numerous micropores. Conversely, type IV isotherms, characteristic of mesoporous materials, feature a distinct plateau at intermediate pressures, indicative of the presence of mesopores. The observed isotherms also exhibited a small hysteresis loop at medium pressure with a gradual decline. This phenomenon is consistent with the formation of a mesoporous structure within the activated carbon sample, indicating the coexistence of micropores and a limited quantity of mesopores [28,29].

Fig. 3 presents the pore size distribution curves obtained through Density Functional Theory (DFT) analysis for activated carbons derived

from cashew nut shells, synthesized at various activation temperatures (800–900 °C). In this study, a non-local density functional theory (NLDFT) model was utilized, employing the N_2 and CO_2 adsorption-desorption isotherm at −196 °C and 0 °C, respectively, to ascertain the pore size distributions. A comprehensive analysis of the pore structure parameters detailed in Table 2 unveiled intriguing insights: an elevation in both micropore and mesopore counts within the activated carbon as the activation temperature escalated, particularly up to 850 °C. The rise in activation temperature prompted an increase in volatile content, consequently augmenting the micropore volume. Across all samples, the pore size distribution predominantly clustered within the ranges of 0.4–0.7 nm, 0.8–1.0 nm, and 1.1–1.5 nm. Remarkably, the micropore volume, encompassing pores less than 2 nm, exhibited a pronounced predominance, corroborating the findings from N_2 adsorption-desorption isotherm analyses. Notably, the presence of mesopores was less prominent, as evident by the absence of a distinct peak corresponding to mesopores in the pore size distribution curves. Only a minor peak above 1.5 nm hinted at their limited occurrence. Furthermore, pores exceeding 2 nm were notably absent, underscoring the predominantly microporous nature of the activated carbon samples.

Table 2 provides a comprehensive overview of the pore structure parameters characterizing the activated carbon samples derived from cashew nut shells. These parameters, including specific surface area (SSA$_{BET}$), total pore volume (V$_{total}$), micropore volume (V$_{micro}$), and pore width, offer valuable insights into the material's adsorption properties, which are influenced by the activation temperature during synthesis. Starting with AC800, activated at 800 °C, the observed SSA of 1051 m^2/g indicates a substantial surface area available for adsorption. This increase in SSA can be attributed to the creation of micropores and mesopores during the activation process, as the relatively moderate temperature allows for controlled pore formation. Additionally, the average pore width of 1.50 nm reflects the predominance of micropores within the material, which contributes significantly to its adsorption capacity. Upon increasing the activation temperature to 850 °C for AC850, a substantial enhancement in SSA to 1972 m^2/g was observed. This increase in SSA can be attributed to the intensified activation process at higher temperatures, leading to the development of a more extensive network of pores. Consequently, the higher total pore volume of 0.847 cm^3/g and micropore volume of 0.724 cm^3/g further underscore the increased adsorption capacity achieved through temperature elevation. The slight increase in average pore width to 1.55 nm reflects the widening of pores within the material due to the higher activation temperature. Conversely, for AC900 activated at 900 °C, a slight reduction in SSA to 1594 m^2/g was noted compared to AC850. This decline may be attributed to the excessive activation at higher temperatures, leading to the closure or collapse of some pores. Nonetheless, the material still maintains a considerable SSA, indicative of its high
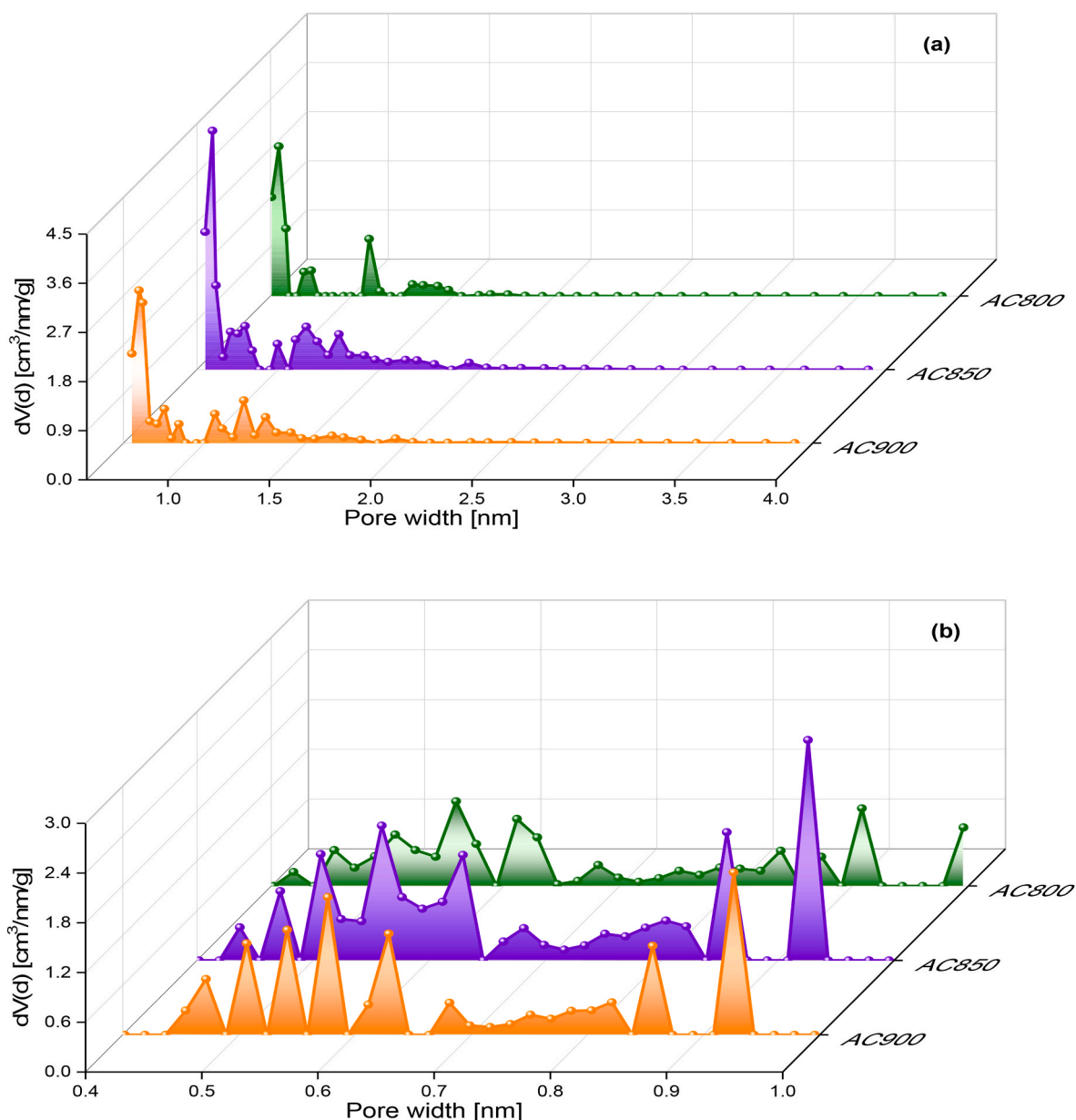
Fig. 3. DFT pore size distributions of activated carbons based on a) N_2 adsorption −196 °C, b) CO_2 adsorption at 0 °C.

Table 2
Textural parameters of the bioorganic prepared activated carbons.

AC sample	SSA_{BET}, m^2/g	V_{total}, cm^3/g	Pore size, cm^3/g	V_{micro}, %
AC800	1051	0.448	1.5	0.428
AC850	1972	0.847	1.55	0.724
AC900	1594	0.713	1.52	0.626

adsorption potential. The relatively consistent average pore width at 1.52 nm suggests the preservation of the predominant microporous structure despite the temperature increase. Overall, the observed trends in SSA, pore volumes, and pore widths underscore the critical influence of activation temperature on the pore structure and adsorption properties of activated carbons. Higher activation temperatures generally lead to increased SSA and pore volumes, facilitating greater adsorption capacities. However, excessive temperatures can also lead to pore collapse or closure, impacting the material's adsorption performance. Therefore, careful control of the activation temperature is essential to optimize the

pore structure and maximize adsorption efficiency [30–32].

3.2. Elemental composition

The specific changes in the elemental composition of the activated carbons, as shown in Table 3, underscore the activation process's efficacy in modifying the materials' textural properties. These findings are consistent with literature reports on activated carbons derived from various biomass sources, where similar trends in elemental composition are observed [33,34]. The highest carbon content, equal to 96.7 wt %,

Table 3
Activated carbons elemental analysis.

AC Sample	C (wt%)	H (wt%)	N (wt%)	O^a (wt%)	O/C Ratio
AC800	92.6	2.2	0.5	4.7	0.05
AC850	96.7	1.3	0.1	2.3	0.02
AC900	94.2	1.8	0.3	3.7	0.04

[a] Calculated by difference.

was obtained for the AC850 sample. The observed minor value of the O/C ratio equal to 0.02 indicates the development of an aromatic structure due to the removal of hydrogen and oxygen from the material [35,36]. This reduction in oxygen content is indicative of a higher degree of carbonization, which enhances the material's stability and adsorptive properties.

3.3. Fourier-transform infrared spectroscopy (FT-IR)

Fig. 4 shows the FT-IR spectra for activated carbons AC-800, AC-850, and AC-900, revealing various functional groups present on their surfaces, which evolve with increasing activation temperatures. A broad peak around 3400 cm^{-1} is observed in all three samples, indicative of O–H stretching vibrations. This is characteristic of hydroxyl groups such as alcohols, phenols, or adsorbed water. The intensity of this peak tends to decrease with increasing activation temperature, suggesting a reduction in hydroxyl groups or adsorbed water as the temperature rises. Hydroxyl groups can influence hydrogen adsorption through hydrogen bonding interactions (H$_2$O–H). Therefore, a reduction in these groups at higher temperatures might lead to a decrease in the hydrogen adsorption capacity through this mechanism [37]. Peaks at approximately 2920 cm^{-1} and 2850 cm^{-1} are consistently present in all samples. These are attributed to C–H stretching vibrations, indicating the presence of aliphatic groups. The consistent presence of these peaks across the samples suggests that aliphatic hydrocarbons remain stable across the different activation temperatures. Aliphatic groups (CH$_2$) are generally less involved in hydrogen adsorption compared to other functional groups like hydroxyl or carbonyl groups. Therefore, their stability suggests that the primary changes affecting hydrogen adsorption occur elsewhere in the chemical structure [38]. A sharp peak in the range of 1700–1720 cm^{-1} is prominent in all spectra, indicative of C=O stretching vibrations. This peak is associated with carbonyl groups such as ketones, aldehydes, and carboxylic acids. Notably, the exact position of this peak shifts slightly to higher wavenumbers (from 1700 cm^{-1} in AC800 to 1720 cm^{-1} in AC900), suggesting an increasing prominence of carbonyl functionalities with higher activation temperatures. Carbonyl groups (C=O) can enhance hydrogen adsorption through dipole-induced interactions, making the increase in these groups at higher temperatures potentially beneficial for hydrogen adsorption. A peak around 1600-1620 cm^{-1} is observed in all samples, likely due to C=C stretching vibrations from aromatic structures or adsorbed water.

This peak's presence indicates that aromatic structures are a significant component of the activated carbons' chemical makeup. Aromatic structures provide a π-electron system that can interact with hydrogen molecules, contributing to adsorption. The persistence of these structures across all samples suggests a stable potential for hydrogen adsorption through π-complexation mechanisms (C=C–H$_2$) [39]. The peak at approximately 1380 cm^{-1} can be attributed to O–H bending vibrations or C–H bending vibrations in aliphatic groups. The consistency of this peak across all samples suggests that hydroxyl groups and aliphatic structures are present in all activated carbons, though the intensity may vary slightly with temperature. The presence of hydroxyl groups, even if reduced, still supports some level of hydrogen bonding interactions, contributing to hydrogen adsorption. A peak around 1050 cm^{-1} is noted in all spectra, associated with C–O stretching vibrations. This is indicative of alcohols, ethers, or carboxylic acids. The presence of this peak in all samples suggests that these oxygen-containing groups are a common feature in the activated carbons, regardless of the activation temperature. Oxygen-containing groups (C–O) can enhance hydrogen adsorption through various interactions, including hydrogen bonding and dipole interactions, thus contributing positively to the adsorption capacity [40].

These observations highlight the impact of activation temperature on the chemical composition and surface functionalities of the activated carbons and their implications for hydrogen adsorption. As the temperature increases, there is a noticeable transformation in the chemical structure, including a reduction in hydroxyl groups and a more prominent presence of carbonyl groups.

3.4. Raman spectroscopy

Fig. 5 shows the Raman spectra of the ACs prepared at different temperatures, providing a nuanced spectroscopic fingerprint that enables detailed characterization of the carbon bonding configurations within the activated carbon. The appearance of the D peak, corresponding to disordered regions, and the G peak, associated with ordered graphitic structures, collectively reveal the intricate interplay of molecular arrangements defining the heterogeneous nature of the microstructure of the activated carbon [41,42]. The data presented offers insight into the microstructural characteristics of the activated carbon samples, elucidated through the discernment of distinct D and G peaks in their Raman spectra. These peaks serve as indicative markers of the
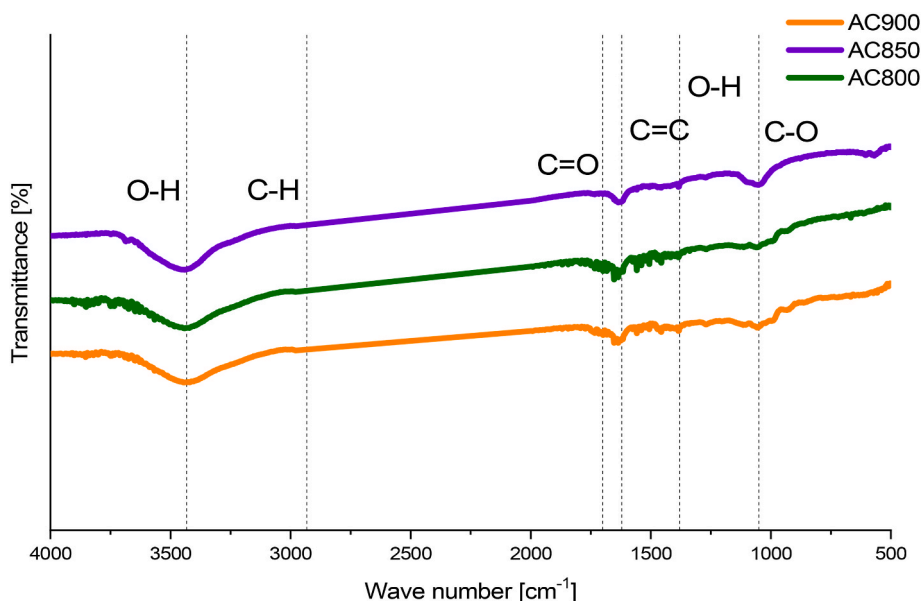

Fig. 4. FTIR spectra for the sample activated at 800 °C, 850 °C and 900 °C.
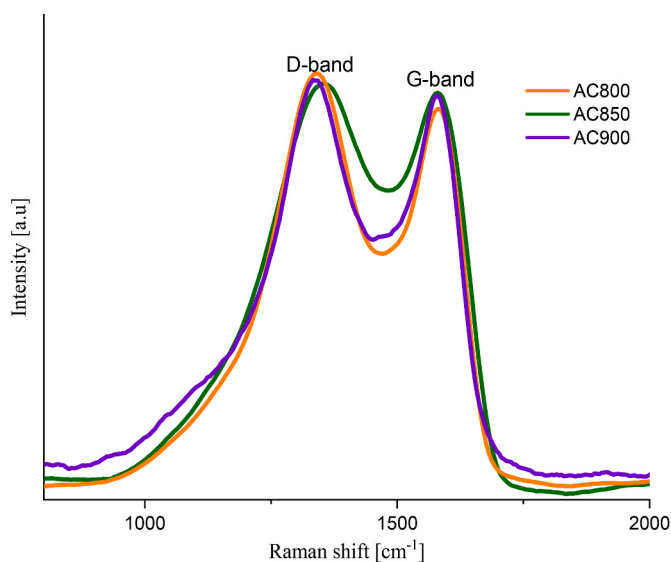
Fig. 5. Raman spectra for the samples activated at 800 °C, 850 °C and 900 °C.

Fig. 6. XRD patterns of a) AC800, b) AC850, c) AC900.

material's heterogeneous microstructure, with the D peak arising from the vibration of carbon-carbon sp2 bonds, indicating disorder or structural irregularities. Conversely, the G peaks result from the vibration of sp2 carbon bonds within an ordered structure akin to graphite [43].

A more detailed analysis involves evaluating the degree of disorder within the carbon matrices, quantified through the intensity ratio of the D peak to the G peak (I_D/I_G) (Table 2). Across the spectrum of elaborated activated carbons, this ratio falls within the range of 0.83–0.87, a range recognized by previous studies as characteristic of non-ordered carbon materials. Notably, higher values within this range indicate an increased presence of aromatic rings and a reduced occurrence of carbon-containing structural defects, fostering the formation of functional groups on the material's surface, often involving oxygen atoms [44]. Furthermore, the I_G/I_D ratio, representing the degree of graphitization, was analyzed alongside the I_D/I_G ratio. A higher I_G/I_D ratio suggests a higher degree of ordered graphitic structures within the material, typically associated with well-defined graphitic layers seen in more ordered carbon materials such as graphite (Table 4). The dependency of these ratios on synthesis temperature was investigated, revealing interesting trends. An increase in synthesis temperature led to a decrease in the I_D/I_G ratio and an increase in the I_G/I_D ratio. This is consistent with expectations, as higher temperatures favor the growth of graphitic domains and promote the formation of ordered graphitic structures, thus reducing disorder within the carbon structure [45].

3.5. X-ray diffraction (XRD)

Fig. 6 shows distinctive peaks, some of which are labeled with Miller indices like (002) and (101). These indices denote the orientation of crystal planes within the carbon structure that are responsible for the diffraction. The (002) peak is indicative of the interlayer spacing in graphitic materials, typically associated with the stacking of graphene layers. The intensity and sharpness of this peak can give insights into the

degree of graphitization; higher and sharper peaks suggest a well-ordered graphitic structure, whereas lower and broader peaks suggest a more amorphous carbon structure or the presence of defects and disorder. As the activation temperature increases from AC800 to AC900, the notable decrease in intensity and increase in the broadening of the (002) peak suggest that the carbon structure is becoming less ordered, which can be attributed to the destruction of graphitic domains or changes in the turbostratic arrangements of the carbon layers. This could result in an increase in the amorphous phase, potentially enhancing the material's porosity and specific surface area, which are desirable for applications that require high adsorption capacity. The (101) peak also provides information on the crystalline structure, and its variation with activation temperature further supports the notion that the carbon is undergoing structural changes. The broadening of this peak across the temperatures suggests an increase in lattice defects or a transformation of the crystalline structure towards a more amorphous state.

Table 4
Summary of Raman spectra analysis for activated carbon samples at different synthesis temperatures.

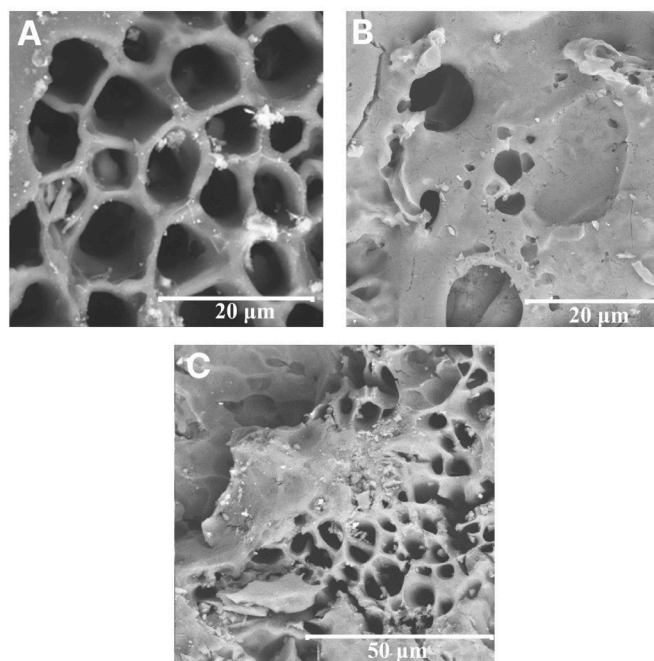| AC Sample	D peak frequency (cm^{-1})	G peak frequency (cm^{-1})	I_D/I_G	I_G/I_D
AC800	1392.3	1594.6	0.87	1.15
AC850	1333.0	1600.3	0.83	1.20
AC900	1337.1	1584.9	0.84	1.19

Fig. 7. SEM images of a) AC800, b) AC850, c) AC900.

3.6. Scanning electron microscope (SEM)

Fig. 7 presents a detailed examination of the pore structures of activated carbon surfaces using SEM micrographs. The images primarily reveal the mesoporous and macroporous networks within the carbonaceous structures. The presence of micropores in the activated carbon samples has been confirmed through nitrogen adsorption-desorption isotherms at −196 °C, as shown in Table 2. These analyses indicate a significant microporous structure, which is crucial for high-performance gas adsorption. This open pore structure is crucial for gas adsorption applications, particularly for the efficient and selective adsorption of H_2 molecules. The unobstructed pore pathways facilitate optimal gas adsorption performance by ensuring unhindered access to the pore space, thus promoting effective gas-surface interactions. Examination of the surface morphology across these activated carbon samples shows consistent macroporous structures, despite variations in activation temperatures during synthesis. This uniformity in pore architecture is vital for gas adsorption applications. The consistent morphology suggests that while activation temperatures impact microstructural features, they do not significantly alter the broader macroporous architecture. This consistency ensures reliable and reproducible gas adsorption behavior across diverse samples, highlighting the potential of these activated carbons for use in gas separation and storage systems. The activated carbon derived from nut biomass demonstrates a promising pore structure suitable for gas adsorption applications, as supported by previous studies. The potential of biomass-derived activated carbons for hydrogen storage and gas separation is an exciting prospect, offering a sense of excitement and anticipation for the audience. Similar results were achieved by Chairunnisa et al. [41] and Serafin et al. [42].

3.7. Thermogravimetric (TGA) analysis

The thermogravimetric analysis (TGA) of untreated cashew nutshell has revealed detailed information on the complex thermal breakdown processes of this biomaterial, as given in Fig. 8. Beginning with the TGA curve, there's a gradual decline in weight percentage from room temperature up to approximately 100–150 °C, which is typically associated with the evaporation of moisture within the biomass. This initial weight loss is minor compared to the subsequent losses. As the temperature rises beyond this point, the TGA curve shows a more pronounced weight loss, which corresponds to the main decomposition phase of the biomass components. This is where the DTG curve becomes particularly informative. The DTG peaks represent temperatures at which the rate of weight loss is greatest, indicating the breakdown of the primary components of the biomass:

- The first peak in the DTG curve likely corresponds to the decomposition of hemicellulose, which generally occurs at lower temperatures than cellulose and lignin, around 200–300 °C.
- A sharp peak usually signifies cellulose breakdown, typically between 300 and 400 °C. Cellulose has a higher thermal stability and decomposes at a relatively specific temperature range, leading to a distinct peak in the DTG curve.
- Lignin decomposition is more gradual and extends over a wide temperature range, often starting around 200 °C and continuing well beyond 500 °C. As lignin has a complex structure that breaks down in stages, this could result in a broader peak or multiple peaks in the DTG curve.

After the major decomposition phase, the TGA curve levels off, indicating a significant slowdown in weight loss. This plateau suggests the formation of char, which is the carbonaceous residue remaining after the volatile components have been driven off. The DTG curve also flattens out, showing that the rate of weight loss has decreased significantly. Further decomposition of the char and any residual material can continue up to 800 °C but at a much slower rate. From the TGA and DTG graph, we can deduce that the cashew nutshell biomass exhibits a typical decomposition pattern for lignocellulosic materials, with distinct phases for moisture loss, active devolatilization from the breakdown of hemicellulose, cellulose, and lignin, and finally, char degradation.

The TGA and DTG curves for activated carbons at different preparation temperatures reveal distinct thermal stability characteristics, as presented in Fig. 9. The ACs exhibit a clear pattern of thermal behavior. Initial weight loss across the range is consistent, likely from moisture release. As temperature increases, the TGA curves show separation, with the AC800 sample having more volatile content as evidenced by a higher DTG peak, compared to the lower peaks of AC850 and AC900, indicating a decrease in volatile matter for carbons prepared at higher temperatures. The DTG peaks are most pronounced around 200 °C–500 °C, corresponding to the release of organic components. Above 600 °C, the curves level off, showing significantly less weight loss, with AC900 displaying the greatest thermal stability and highest residual weight, implying that carbon prepared at 900 °C has the most robust carbon structure with the highest fixed carbon content. This suggests that carbons subjected to higher preparation temperatures undergo more thorough carbonization, resulting in less volatile and more stable activated carbon materials.

3.8. H_2 adsorption tests

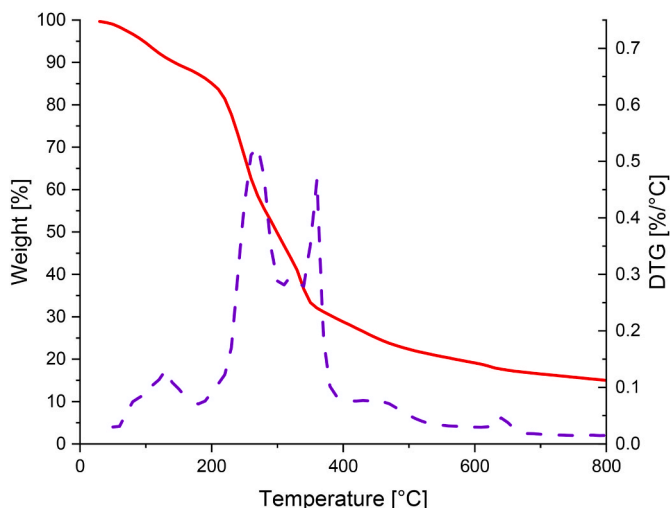The low-pressure hydrogen adsorption isotherm (Fig. 10(a))
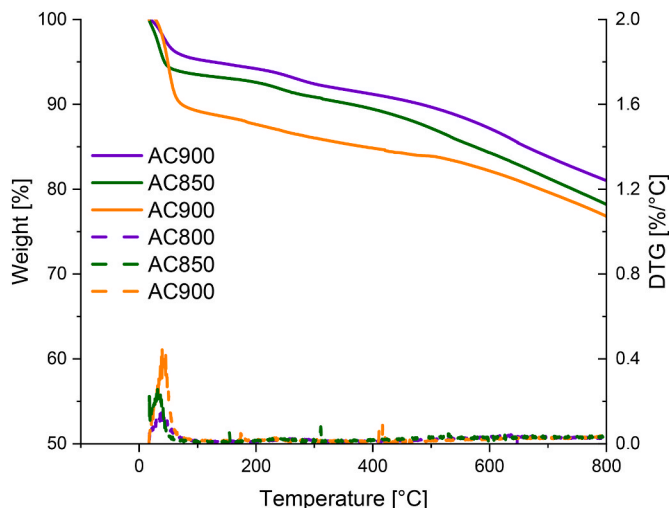

Fig. 8. TGA of raw CNS.

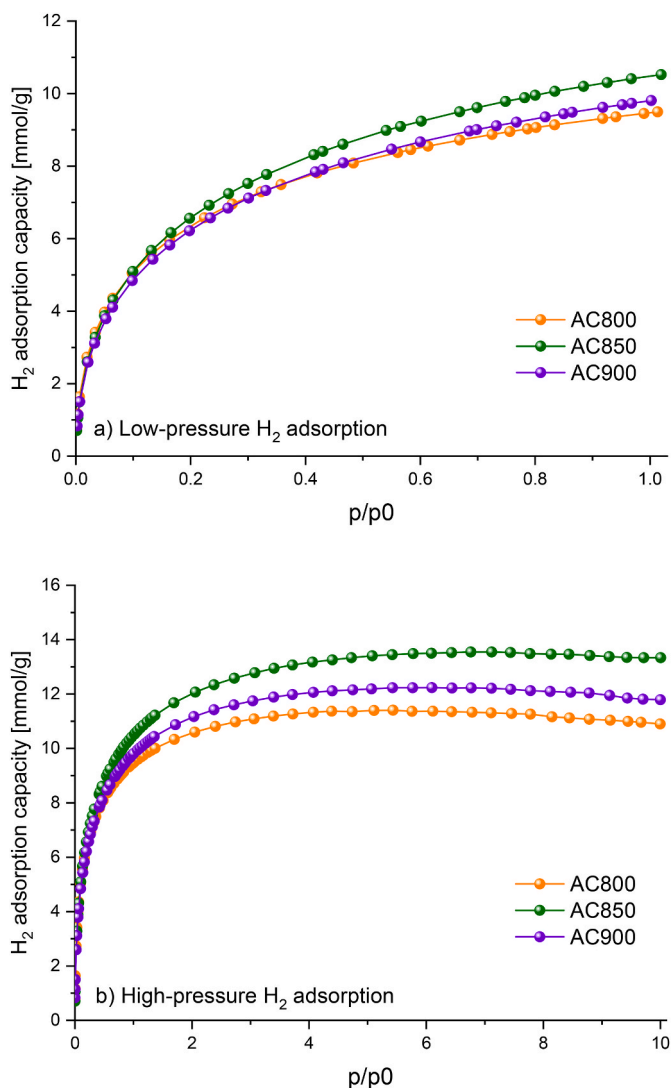**Fig. 9.** TGA of activated carbons produced from CNS.

Fig. 10. H$_2$ (a) low-pressure (b) high-pressure isotherms of measured at 25 °C in the range of 0–10 bar.

illustrates the relationship between the adsorption capabilities of materials AC800, AC850, and AC900, and the relative pressure (p/p$_0$). The behavior of all materials follows Type I isotherms, which are typical of microporous solids. In these isotherms, the adsorption capacities increase significantly at low pressures because of the intense contact between hydrogen molecules and the surface of the adsorbent. The sharp incline at the beginning suggests that the adsorption process has favorable energy characteristics at low pressures, making it advantageous for applications that function under gentle circumstances. As the relative pressure approaches p/p$_0$ = 1, the adsorption isotherms reach a plateau, indicating saturation. AC850 has the greatest adsorption capacity, approaching 10.52 mmol/g (2.12 wt%), indicating a substantial surface area (1972 m^2/g), improved total pore (0.847 cm^3/g) and micropore volume (0.724 cm^3/g) in comparison to AC800 and AC900. The AC800 isotherm exhibits a slight change in direction at p/p$_0$ = 0.4, suggesting the possible existence of mesopores or a non-uniform distribution of pores. This characteristic might enhance the material's ability to facilitate diffusive transport.

Fig. 10(b) expands the investigation to high-pressure circumstances, including relative pressures up to p/p$_0$ = 10. The isotherms maintain a Type I pattern, but the adsorption capacities at high pressures far surpass those reported at lower pressures. Specifically, the AC850 sample has an adsorption capacity above 13.34 mmol/g (2.69 wt%). The significant

rise indicates that these materials possess advantageous adsorption properties even at high pressures, which is crucial for applications involving the storage of hydrogen at high densities. The isotherms of each material exhibit various points of stabilization, with AC850 reaching a plateau at a lower relative pressure compared to AC800 and AC900. This suggests that the hydrogen molecules are packed more efficiently inside the pore structure of AC850, owing to a more ideal distribution of pore sizes or a stronger material framework that remains stable when compressed.

Table 5 presents a summary of the findings on H$_2$ adsorption using various adsorbents, including those derived from diverse biomass sources. The results obtained in this work are potentially competitive compared to other solid carbon-based materials. The physicochemical structure of these materials significantly influences their hydrogen storage and gas separation performance. Key factors include:

- Pore size distribution: Micropores (<2 nm) increase hydrogen storage capacity due to a high surface area and volume.
- Surface functional groups: Functional groups such as hydroxyl and carbonyl groups can enhance adsorption affinity.
- Degree of graphitization: Higher graphitization levels improve structural stability and reusability.
- Textural properties: A balance of micro and mesopores facilitates efficient gas diffusion and adsorption.

3.9. Isosteric heat of H$_2$ adsorption

The isosteric heat of H$_2$ adsorption was calculated for 0 (Fig. 11) and 25 °C (Fig. 10(b)) and acts as a definitive measure of the intensity of contact between the adsorbate and the adsorbent surface, as given by the Clausius-Clapeyron equation:

$$Q_{st} = - R \left(\frac{\partial(\ln(p))}{\partial\left(\frac{1}{T}\right)} \right)_{\theta} \tag{5}$$

where: p is the partial pressure of the H$_2$ at equilibrium state [bar], T is absolute temperature [K], R is the ideal gas constant [J/mol·K], Q$_{st}$ denotes isosteric heat of adsorption [J/mol], and θ indicates a specific surface coverage [−].

The pressure values for the given surface coverage have been calculated using the modified Langmuir-Freundlich isotherm equation, which has been shown to be effective for this particular use [52].

Table 5
Comparison of H$_2$ uptakes of various carbon-based materials.

| Adsorbent	Experimental conditions		H$_2$ uptake, mmol/g/wt. %	Reference
	Pressure, bar	Temperature, °C		
Wood chips-based ACs	80	25	2.48/0.50	[46]
SWCNT	0.4	25	22.32/4.50	[47]
MWCNT	14.8	25	31.25/6.31	[47]
K-doped MWCNT	0.1	<40	8.93/1.80	[48]
10 wt% Pd-AC	60	30	2.63/0.53	[49]
Tangerine peel-based ACs	30	25	0.69/0.14	[50]
CO$_2$-oxidized MWCNTs	120.5	25	4.46/0.90	[51]
Air-oxidized MWCNTs	120.2	25	4.96/1.00	[51]
Common polypody-based ACs	45	25	9.61/1.94	[54]
Cashew nut shells-based ACs	10	25	13.34/2.69	This work
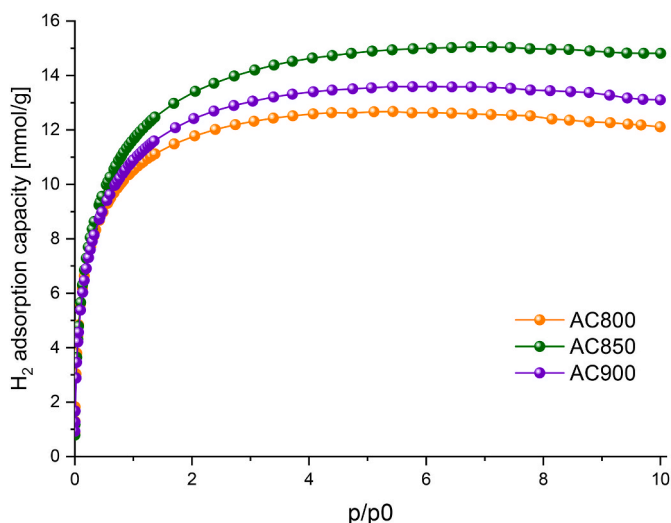
Fig. 11. H$_2$ isotherms measured at 0 °C in the range of 0–10 bar.

$$p(n) = \sqrt[n_{FL}]{\frac{q_e}{q_m \bullet K_{FL} - q_e \bullet K_{FL}}} \qquad (6)$$

Where: q$_m$ - maximum adsorption capacity (cm^3/g), K$_{FL}$ - Langmuir-Freundlich isotherm constant (bar^{-1}), n$_{FL}$ - index of heterogeneity [−]

The isosteric heat of adsorption ACs was found to vary from 6.56 to 4.39 kJ/mol, in proportion to the total surface coverage, as shown in Fig. 12. The result offers strong verification that the adsorption of H$_2$ on ACs is a physical process that is regulated by relatively weak van der Waals forces. Physical adsorption has a relatively low Qst, ranging from 20 to 40 kJ/mol, while the heat of chemisorption often falls within the range of 80–200 kJ/mol [53]. Similar results for H$_2$ storage on ACs have been achieved by Serafin et al. [54] for different raw material.

3.10. Modelling of H$_2$ adsorption processes

Modeling of H$_2$ adsorption isotherms on AC800, AC850, and AC900 materials were studied to analyze their adsorption characteristics up to 10 bar, as given in Fig. 13(a–c). The Langmuir (SSE: 17.68–26.32). And Freundlich (SSE: 70.50–77.12) isotherms did not accurately model the adsorption behavior across the pressure spectrum, suggesting limitations due to their assumptions of monolayer adsorption and surface heterogeneity, respectively. The Temkin isotherm (SSE: 24.08–25.64)
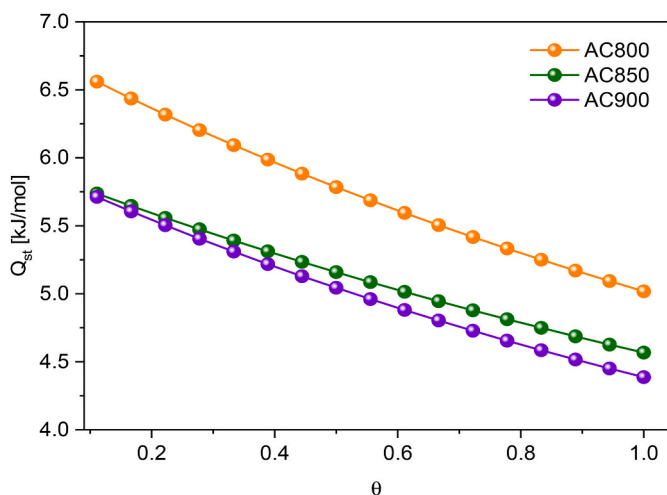
Fig. 12. Change of the isosteric heat of H$_2$ adsorption as a function of surface coverage for the prepared ACs.
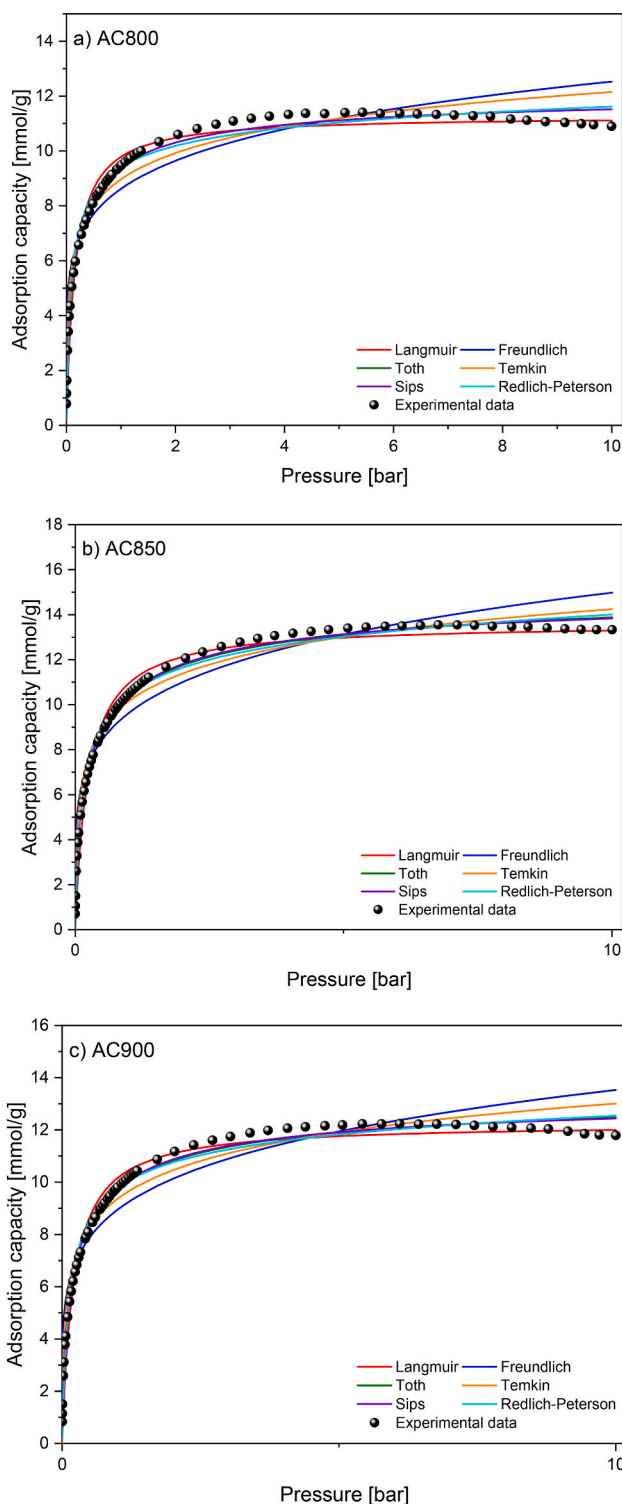
Fig. 13. Fitting of H$_2$ adsorption isotherms to selected models for (a) AC800, (b) AC850, and (c) AC900 at 25 °C.

also fell short, indicating that adsorbate-adsorbent interactions are not dominant within the studied pressure range. Conversely, Sips (SSE: 3.05–4.46) and Toth (SSE: 4.78–6.15) equations were two of the six remaining isotherm models that may effectively describe the H$_2$ adsorption capabilities of ACs. Generally, the Toth model improves on the Langmuir isotherm by accounting for varied adsorption sites, enhancing fit at high pressures where Langmuir fails, suggesting diverse adsorption energies due to site differences. The Sips isotherm, merging

Langmuir and Freundlich models, best matches experimental data across all pressures for three materials, accommodating surface heterogeneity and aligning with the Langmuir isotherm at high pressures, effectively explaining adsorption in mixed-surface systems. Similarly, the Redlich-Peterson (SSE: 10.40–11.31) isotherm, a three-parameter model combining the Langmuir and Freundlich isotherms, also provided a good fit but not as precise as the Sips and Toth equations.

The excellent performance of the Sips and Toth isotherms in depicting hydrogen adsorption data indicates that these models' incorporation of surface heterogeneity and fluctuation in adsorption energy are crucial for accurately characterizing adsorptive behaviors. The parameter estimates derived from these models may provide useful insights into the characteristics of the adsorption sites and the interaction energies. This information is crucial for enhancing the design and advancement of adsorbent materials used in hydrogen storage applications.

3.11. H_2, CO_2, and CH_4 selectivity studies

3.11.1. Equimolar combinations of H_2/CO_2, H_2/CH_4, and CO_2/CH_4

Adsorbent materials play a crucial role in the selective separation of components in gaseous mixtures containing hydrogen (H_2), carbon dioxide (CO_2), and methane (CH_4). The selectivity of these materials is critical for various applications, including gas purification, carbon capture, and energy storage. Analyzed the adsorption isotherms of $H_2/CO_2/CH_4$ at 25 °C for the best sample (AC850) to determine the selectivity between those three gases. This study calculated the gas selectivity of $H_2/CO_2/CH_4$ by using the ideal adsorption solution theory (IAST) to accurately assess the efficiency of the separation process.

The IAST method, created by Myers and Prausnitz, is widely used to calculate the adsorption selectivity of gas mixtures in porous materials [55]. This integration adheres to a certain equation of state to ensure a precise evaluation.

$$S_{IAST} = \frac{q_{X(p)}}{q_{Y(p)}} \bullet \frac{p_Y}{p_X} \qquad (7)$$

where: S_{IAST} is the selectivity coefficient, $q_{X(p)}$ and $q_{NY(p)}$ refer to the uptake of specific gas [mmol/g], p_X and p_Y are the partial pressure in the mixture.

As a result, our focus was on investigating the selectivity for a H_2/CO_2, H_2/CH_4, or CO_2/CH_4 (0.5/0.5) binary mixture. In this context, equation (1) is modified and expressed in the following specific form:

$$S_{IAST(EQ)} = \frac{q_{CO_2(p)}}{q_{N_2(p)}} \qquad (8)$$

Fig. 14 shows the selectivity data obtained from IAST for equimolar combinations of H_2/CO_2, H_2/CH_4, and CO_2/CH_4 in flue gas at 25 °C. mixtures explore how different gas species interact with the adsorbent surface and compete for adsorption sites under uniform conditions.

➢ **Selectivity Coefficient of CO_2 compared to CH_4**: The selectivity coefficient of CO_2 relative to CH_4 demonstrates a significant range, from 8.4 to 2.0, as pressure increases from 0.01 to 10 bar. At lower pressures, CO_2 exhibits a pronounced preference for adsorption over CH_4, likely due to its larger molecular size and higher polarizability, allowing for stronger interactions with the adsorbent surface. However, as pressure rises, the selectivity coefficient decreases, indicating a reduced preference for CO_2 adsorption over CH_4. This reduction could stem from the saturation of adsorption sites and increased competition between CO_2 and CH_4 molecules for surface binding [56].

➢ **Selectivity Coefficient of H_2 compared to CO_2**: The selectivity coefficient of H_2 relative to CO_2 also shows significant variation, ranging from 11.9 to 1.4, with increasing pressure from 0.01 to 10 bar. Initially, H_2 displays a strong preference for adsorption over
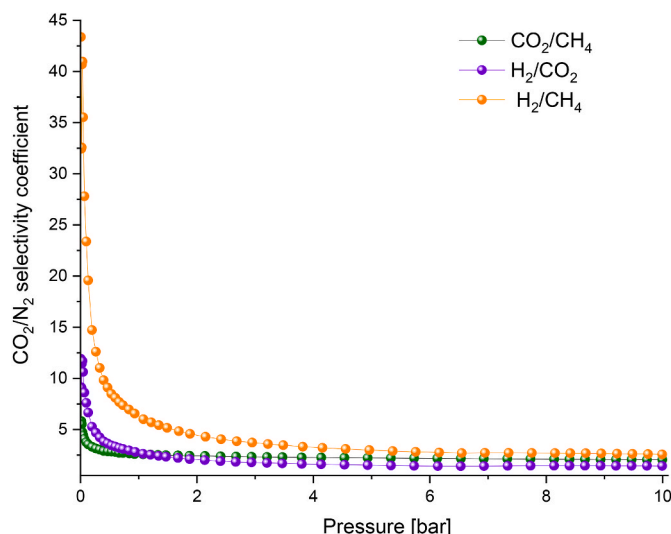

Fig. 14. H_2/CO_2, H_2/CH_4, and CO_2/CH_4 selectivity of AC850 samples versus pressure at 25 °C.

CO_2, likely due to its smaller size and potentially stronger interactions with the adsorbent surface. However, as pressure increases, the selectivity coefficient decreases, indicating a diminishing preference for H_2 adsorption over CO_2. This decrease may result from the saturation of adsorption sites and intensified competition between H_2 and CO_2 molecules for surface adsorption [57].

➢ **Selectivity Coefficient of H_2 compared to CH_4**: The selectivity coefficient of H_2 relative to CH_4 exhibits the most significant variation, ranging from 43.4 to 2.6, as pressure increases from 0.01 to 10 bar. Initially, H_2 demonstrates a strong preference for adsorption over CH_4, attributed to its smaller size and potentially stronger interactions with the adsorbent surface. However, with increasing pressure, the selectivity coefficient decreases markedly, indicating a substantial decrease in the preference for H_2 adsorption over CH_4. This decrease likely arises from the saturation of adsorption sites and intensified competition between H_2 and CH_4 molecules for surface binding [58].

3.11.2. Selectivity for a mixture of three gases (H_2, CO_2, and CH_4) in industrial applications

The selectivity of the gas components within the three-component mixture was meticulously calculated employing the Serafin-Dziejarski method. This methodological approach is predicated on the foundational principles of the Langmuir isotherm equation, tailored to assess, and quantify the selective adsorption characteristics of each gas in the context of a competitive adsorption environment.

The Serafin-Dziejarski selectivity calculations are instrumental in elucidating the efficiency with which the adsorbent differentiates between the gas species under investigation. For each component in the mixture (CH_4, CO_2, H_2), the selectivity is derived from the ratio of the amount of that specific gas adsorbed to the sum of the amounts of the other gases adsorbed, each normalized by their respective partial pressures. This ratio encapsulates the preferential adsorption efficacy of the adsorbent for each gas relative to the others in the mixture, as shown in below equation:

$$S_{\text{Serafin-Dziejarski-X1}} = \frac{\frac{n_{X1}}{P_{X1}}}{\frac{n_{X2} + n_{X3}}{P_{X2} + P_{X3}}} \qquad (9)$$

Where:

- X1 is a gas adsorbed,

- n_{X1} is the amount of X1 gas adsorbed,
- n_{X2} and n_{X2} are the amounts of X2 and X3 gases adsorbed, respectively,
- P_{X1}, P_{X2}, and P_{X3} are the partial pressures of X1, X2, and X3 gas in the mixture, respectively.

The Serafin-Dziejarski selectivity calculations were applied to the following four gas mixture examples to illustrate the method's versatility and applicability in varying industrial contexts, as presented in Tables 6 and 7.

- **H$_2$ selectivity**: Hydrogen has the highest selectivity values in all examples, ranging from approximately 12.60 to 14.14. This suggests that under the conditions studied, hydrogen is preferentially adsorbed over methane and carbon dioxide, likely due to its small molecular size and high mobility.
- **CO$_2$ selectivity**: Carbon dioxide shows moderate selectivity values between approximately 0.65 and 0.72. These values are significantly lower than those of hydrogen, indicating that CO_2 is less preferentially adsorbed compared to H_2. However, CO_2 is more selectively adsorbed than CH_4, likely due to its higher polarizability and interaction with the activated carbon surface.
- **CH$_4$ selectivity**: Methane has the lowest selectivity values, which range from approximately 0.09 to 0.16 across the examples. Methane's larger molecular size compared to hydrogen and its non-polar nature compared to carbon dioxide could contribute to its lower selectivity.

The variation in selectivity across the examples can be attributed to differences in the gas composition, which affects the partial pressures and, consequently, the adsorption behavior according to the Langmuir isotherm equation. These results align with the understanding of porosity and the capability of activated carbons to adsorb smaller molecules more effectively. Activated carbon, with its high surface area and porosity, tends to adsorb gases like hydrogen more readily due to its small molecular size, allowing for higher selectivity. In contrast, larger molecules like methane are less easily accommodated in the microporous structure of activated carbon, resulting in lower selectivity.

3.12. Industrial scalability and economic feasibility aspects

This economic analysis examines the financial viability of producing activated carbon from cashew nut shells, with a specific focus on Vietnam's prominent cashew industry. Vietnam, a leading global producer, generated approximately 1.5 million tons of cashew nuts in 2023, highlighting its crucial role in the industry [59]. The analysis evaluates the costs associated with setting up and operating a production facility in Vietnam, aiming to assess the feasibility of utilizing cashew nut shells—byproducts of the cashew processing sector—for activated carbon production. In addition to Vietnam, other significant producers in the global cashew market include India, Brazil, Nigeria, and Indonesia (Fig. 15).

This study provides insights into the economic practicality of this production method, considering both cost efficiency and waste reduction potential. The establishment of the production facility involves

Table 6

Compositions of gas mixtures.

Example	CH$_4$ [%]	CO$_2$ [%]	H$_2$ [%]	Applications
1	0.8	0.1	0.1	Heating, power generation, or as a feedstock for chemical processes
2	0.7	0.2	0.1	Industrial processes or power generation
3	0.85	0.05	0.1	Clean-burning fuel in residential, commercial, or industrial setting
4	0.75	0.15	0.1	Power generation, or heating

Table 7

Selectivity calculations across four gas mixture examples, employing the Serafin-Dziejarski method.

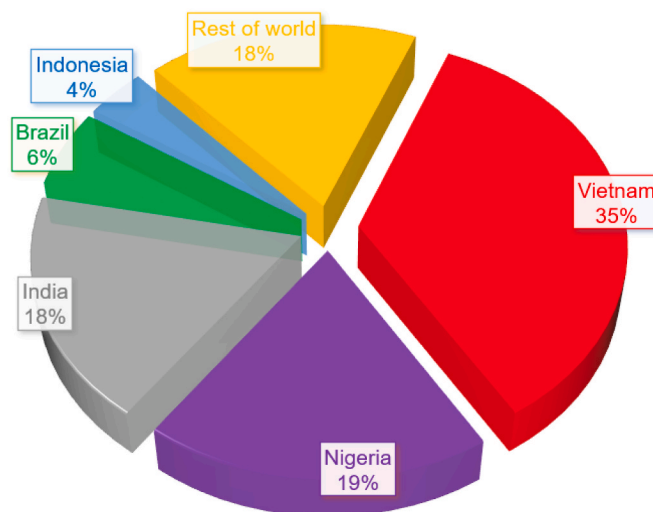| Gas	Example 1	Example 2	Example 3	Example 4
H$_2$	13.59	12.60	14.14	13.07
CO$_2$	0.70	0.65	0.72	0.67
CH$_4$	0.12	0.16	0.096	0.14

Fig. 15. World cashew nuts production.

several key investments, including site preparation, building construction, and the installation of essential machinery. These initial setup activities ensure that the production operations are efficient and effective. Site preparation involves clearing and leveling the land, while building construction includes creating the physical facility to house machinery. The installation of reactors, dryers, grinders, and other specialized equipment is crucial for the activation process. Additionally, architectural and engineering design services are required to optimize the facility layout, and investments in fire safety measures and regulatory permits are necessary to ensure compliance with legal standards.

Table 8 provides all data and values. Establishing a production facility for activated carbon from cashew nut shells involves a wide array of costs that ensure the site is properly equipped and operational. To begin with, the initial cost of facility setup is estimated at 30,000 € (819,074,070 VND). This expense includes the broad range of investments needed to prepare and construct the production site. The cost of construction materials, which is a significant part of the setup expenses, varies between 8000 € and 15,000 € (218,662,560 to 410,993,800 VND). This variability depends on the specific materials used and their quality. Labor costs for the setup phase are estimated to fall between 6000 € and 10,000 € (163,999,680 to 273,328,200 VND). This amount covers the wages of workers who are involved in the construction and installation processes. The design phase, encompassing architectural planning and layout design, costs between 1500 € and 3000 € (41,833,130 to 82,059,870 VND). Technical installations, including essential systems such as plumbing and electrical work, are expected to cost between 2000 € and 3000 € (54,665,520 to 82,059,870 VND). Additional costs for fire safety measures and necessary permits and certificates each range from 300 € to 500 € (8,200,915 to 13,676,645 VND), ensuring that the facility complies with safety regulations and legal requirements. Once the facility is set up, processing the cashew nut shells is a critical step in preparing them for activation. This process involves cleaning, drying, and grinding the shells. Cleaning removes impurities and contaminants from the shells, ensuring they are in the best condition for the subsequent activation process. Drying

Table 8
Costs of industrial production of activated carbon from cashew nut shells.

Cost Component	Estimated Cost (€)	Estimated Cost (VND)
Facility Setup	30,000	819,074,070
Construction Materials	8000–15,000	218,662,560–410,993,800
Labor	6000–10,000	163,999,680–273,328,200
Design	1500–3000	41,833,130–82,059,870
Technical Installations	2000–3000	54,665,520–82,059,870
Fire Safety Measures	300–500	8,200,915–13,676,645
Permits and Certificates	300–500	8,200,915–13,676,645
Process	**Annual Cost (€)**	**Annual Cost (VND)**
Cleaning, Drying, Grinding	2000	54,665,520
Equipment	**Estimated Cost (€)**	**Estimated Cost (VND)**
Horizontal Tube Furnace	12,000	328,195,620
Stainless Steel Reactors	25,000	682,453,250
Drying and Grinding Equipment	12,000	328,195,620
Filtration and Washing Units	5000	136,676,450
Quality Control Instruments	2000	54,665,520
Packaging Machinery	5000	136,676,450
Storage Facilities	15,000	410,996,350
Staff	**Estimated Hourly Rate (€)**	**Estimated Hourly Rate (VND)**
Production Operators	1.50–3.00	41,833,130–82,059,870
Supervisors	3.00–5.00	82,059,870–136,766,450
Support Staff	1.00–1.50	27,353,290–41,530,985
Utility	**Unit Cost (€)**	**Unit Cost (VND)**
Electricity	0.05–0.07 per kWh	1367.67–1915.71 per kWh
Water	0.20–0.30 per m^3	5470.66–8206.00 per m^3
Gas	0.80–1.20 per m^3	21,870.68–32,806.02 per m^3
Maintenance and Repairs	**Annual Cost (€)**	**Annual Cost (VND)**
Maintenance and Repairs	800	21,870,680
Quality Control	**Annual Cost (€)**	**Annual Cost (VND)**
Quality Control	400	10,935,340
Logistics Component	**Annual Cost (€)**	**Annual Cost (VND)**
Storage	800	21,870,680
Transportation and Packaging	1500	41,530,985
Summing up all annual costs, the total production cost	**102,550 € (2,764,654,470 VND)**	

Exchange rate used: 1 Euro (€) = 27,353.29 Vietnamese Đồng (VND)*current exchange value 05/08/2024.

reduces the moisture content, which is crucial for effective activation. Grinding increases the surface area of the shells, enhancing their efficiency during activation. The combined annual cost for these processing steps is approximately 2000 € (54,665,520 VND). The production of activated carbon requires several specialized pieces of equipment, each contributing significantly to the overall investment. A horizontal tube furnace, essential for the carbonization process, costs 12,000 € (328,195,620 VND). Stainless steel reactors, used for chemical activation, are priced at 25,000 € (682,453,250 VND). Equipment necessary for drying and grinding the cashew shells costs another 12,000 € (328,195,620 VND).

To maintain the quality of the final product, filtration and washing units are required, costing 5000 € (136,676,450 VND). Quality control instruments, which ensure that the final product meets industry standards, are estimated at 2000 € (54,665,520 VND). The packaging equipment necessary for preparing the product for distribution costs €5000 (136,676,450 VND). Lastly, storage facilities, essential for holding both raw materials and finished products, are estimated to cost 15,000 € (410,996,350 VND). The total investment in equipment amounts to approximately €76,000 (2,088,592,810 VND), with an annual depreciation cost of 6000 € (163,999,680 VND) spread over a period of 10 years. This significant initial investment is critical for

ensuring that the production process runs smoothly and effectively. A skilled workforce is necessary to manage the production process efficiently. Staffing costs cover the wages of production operators, supervisors, and support staff. Production operators, who handle the machinery and ensure its effective operation, have hourly rates ranging from 1.50 € to 3.00 € (41,833,130 to 82,059,870 VND). Supervisors responsible for overseeing the entire production process and ensuring quality and efficiency are paid between 3.00 € and 5.00 € per hour (82,059,870 to 136,766,450 VND). Support staff, who assist with maintenance and logistics, earn between 1.00 € and 1.50 € per hour (27,353,290 to 41,530,985 VND). The total estimated annual cost for staffing is approximately 12,000 € (327,999,680 VND). The production process is highly energy-intensive, leading to substantial utility expenses. The estimated annual utility costs amount to around 2250 € (55,057,395 VND). Specifically, electricity costs between €750 and 1050 € (20,510,070 to 28,572,160 VND) for an annual consumption of about 15,000 kW h, depending on the unit cost of 0.05 € to 0.07 € per kWh. Water costs range from 500 € to 750 € (13,676,645 to 20,515,380 VND) for annual consumption of approximately 2500 m^3, based on a unit cost of 0.20 € to 0.30 € per m^3. Gas costs between 800 € and 1200 € (21,870,680 to 32,806,020 VND) for annual consumption of around 1000 m^3, depending on the unit cost of 0.80 € to 1.20 € per m^3. Regular maintenance and occasional repairs are vital for the reliable operation of the equipment. The estimated annual cost for maintenance and repairs is 800 € (21,870,680 VND).

Additionally, quality control is essential to ensure that the final product meets industry standards, with an estimated annual cost of 400 € (10,935,340 VND). Efficient logistics management also involves costs related to the storage, transportation, and packaging of raw materials and finished products. The estimated annual logistics costs total approximately 2300 € (63,401,665 VND). This includes storage costs of 800 € (21,870,680 VND) and transportation and packaging costs of 1500 € (41,530,985 VND). In summary, the comprehensive financial requirements for setting up and operating a facility dedicated to producing activated carbon from cashew nut shells encompass various costs, including facility setup, equipment investment, staffing, utilities, maintenance, quality control, and logistics. The total estimated annual production cost amounts to 102,550 € (2,764,654,470 VND).

To determine the cost per kilogram of activated carbon, assuming an annual production volume of 50,000 kg:

$$\text{Price per kiolgram} = \frac{total\ annual\ production\ costs}{\text{annual production volume}} \tag{10}$$

$$\textbf{Price per kiolgram} = \frac{\textbf{102,550 €}}{\textbf{50,000}} = 2.05€ \Big/ \textbf{55,293 VND} \tag{11}$$

This analysis demonstrates that production costs in Vietnam can be effectively managed to achieve a competitive price of approximately 2.05 € per kilogram. By optimizing costs related to facility setup, equipment, staffing, utilities, and logistics, the production process becomes economically viable. Utilizing cashew nut shells as a raw material further enhances cost-effectiveness and supports sustainability. Adhering to quality control standards is essential for product reliability and market competitiveness. Effective financial and operational planning will be crucial for achieving and sustaining profitability in the activated carbon production industry. The resultant production cost of 2.05 € per kilogram is notably competitive when compared to current market prices for activated carbon, which typically range from 2.50 € to 4.00 € per kilogram depending on the type and application. By positioning itself within this cost range, the Vietnam-based production operation can effectively compete with established players in the market, particularly in applications where cost efficiency is a significant factor. This cost advantage, coupled with the sustainable use of raw materials, provides a strong foundation for capturing market share and achieving long-term profitability.

4. Conclusions

The study presents a promising advancement in the utilization of agricultural waste for environmental and industrial applications, specifically through the development of activated carbon from cashew nut shells using potassium hydroxide activation. The research further employs advanced characterization techniques, including N_2/CO_2 adsorption isotherms, FT-IR, Raman spectroscopy, XRD, SEM, and TGA, to investigate the structural and chemical characteristics of the produced activated carbon. These methods reveal detailed insights into the functional groups and molecular structure of the activated carbon, as well as its thermal stability and composition. The findings emphasize the potential of using cashew nut shells, a form of agricultural waste, to develop efficient materials for environmental and industrial applications. The study's key findings and implications are summarized as follows:

- Development of activated carbon from cashew nut shells using potassium hydroxide activation demonstrates a promising use of agricultural waste.
- The AC850 sample exhibits a specific surface area of 1972 m^2/g, suitable for high-pressure gas adsorption applications, especially hydrogen storage.
- Exceptional hydrogen sorption capabilities, with uptake values of 13.34 mmol/g (2.69 wt%) at 10 bar and 25 °C, indicate the material's potential for hydrogen storage and purification.
- Notable H_2/CH_4 selectivity range (43.4–2.6) supports its use in gas purification, particularly for separating hydrogen from methane.
- The activated carbon shows preferential adsorption of hydrogen over carbon dioxide and methane, with carbon dioxide showing moderate selectivity and methane the lowest.

Furthermore, the study of industrial scalability and economic feasibility aspects highlights the cost-effective potential of using cashew nut shells for developing efficient adsorbent materials for environmental and industrial applications. Additionally, the research supports the scalability and economic feasibility of producing high-capacity adsorbents, which could contribute significantly to sustainable energy solutions and gas purification systems.

CRediT authorship contribution statement

Jarosław Serafin: Writing – review & editing, Writing – original draft, Visualization, Validation, Project administration, Formal analysis, Data curation, Conceptualization, Investigation, Methodology, Supervision. **Bartosz Dziejarski:** Writing – review & editing, Writing – original draft, Visualization, Formal analysis, Data curation, Investigation, Methodology. **Óscar Javier Fonseca-Bermúdez:** Writing – original draft, Investigation, Data curation, Funding acquisition, Methodology, Validation. **Liliana Giraldo:** Supervision, Resources, Writing – review & editing. **Rocío Sierra-Ramírez:** Supervision, Resources, Writing – review & editing. **Marta Gil Bonillo:** Formal analysis, Data curation. **Ghulam Farid:** Writing – original draft. **Juan Carlos Moreno-Piraján:** Supervision, Conceptualization, Resources, Writing – review & editing.

Declaration of competing interest

The authors declare that they have no known competing financial interests or personal relationships that could have appeared to influence the work reported in this paper.

Acknowledgements

References

[1] Serafin J, Dziejarski B. Activated carbons—preparation, characterization and their application in CO2 capture: a review. Environ Sci Pollut Control Ser 2023:1–55.
[2] Eberle U, Felderhoff M, Schueth F. Chemical and physical solutions for hydrogen storage. Angew Chem Int Ed 2009;48:6608–30.
[3] Mashhadimoslem H, Ghaemi A, Maleki A, Elkamel A. Enhancement of oxygen adsorption using biomass-based oxidized porous carbon. J Environ Chem Eng 2023;11:109300.
[4] Nazir G, Rehman A, Hussain S, Aftab S, Heo K, Ikram M, Patil SA, Aizaz Ud Din M. Recent advances and reliable assessment of solid-state materials for hydrogen storage: a step forward toward a sustainable H2 economy. Adv Sustainable Sys 2022;6:2200276.
[5] Rimza T, Saha S, Dhand C, Dwivedi N, Patel SS, Singh S, Kumar P. Carbon-based sorbents for hydrogen storage: challenges and sustainability at operating conditions for renewable energy. ChemSusChem 2022;15:e202200281.
[6] Singh G, Lakhi KS, Sil S, Bhosale SV, Kim I, Albahily K, Vinu A. Biomass derived porous carbon for CO2 capture. Carbon 2019;148:164–86.
[7] Serafin J, Dziejarski B, Sreńscek-Nazzal J. An innovative and environmentally friendly bioorganic synthesis of activated carbon based on olive stones and its potential application for CO2 capture. Sustain Mat Tech 2023;38:e00717.
[8] Samsuri A, Sadegh-Zadeh F, Seh-Bardan B. Characterization of biochars produced from oil palm and rice husks and their adsorption capacities for heavy metals. Int J Environ Sci Technol 2014;11:967–76.
[9] Cui X, Jia F, Chen Y, Gan J. Influence of single-walled carbon nanotubes on microbial availability of phenanthrene in sediment. Ecotoxicology 2011;20: 1277–85.
[10] Huang Y, Zhao G. Preparation and characterization of activated carbon fibers from liquefied wood by KOH activation. Holzforschung 2016;70:195–202.
[11] Khadhri N, Saad MEK, ben Mosbah M, Moussaoui Y. Batch and continuous column adsorption of indigo carmine onto activated carbon derived from date palm petiole. J Environ Chem Eng 2019;7:102775.
[12] Mishra S, Mishra A, Khan MA. Decolourization of pulp and paper mill effluents using heat-treated coal: a comparison with activated charcoal. Environ Chem Lett 2010;8:231–5.
[13] Crini G, Lichtfouse E, Wilson LD, Morin-Crini N. Conventional and non-conventional adsorbents for wastewater treatment. Environ Chem Lett 2019;17: 195–213.
[14] Klasson KT, Ledbetter CA, Uchimiya M, Lima IM. Activated biochar removes 100% dibromochloropropane from field well water. Environ Chem Lett 2013;11:271–5.
[15] Jolly G, Dupont L, Aplincourt M, Lambert J. Improved Cu and Zn sorption on oxidized wheat lignocellulose. Environ Chem Lett 2006;4:219–23.
[16] Prauchner MJ, Sapag K, Rodríguez-Reinoso F. Tailoring biomass-based activated carbon for CH4 storage by combining chemical activation with H3PO4 or ZnCl2 and physical activation with CO2. Carbon 2016;110:138–47.
[17] Cruz-Reina LJ, Flórez-Rojas JS, López GD, Herrera-Orozco I, Carazzone C, Sierra R. Obtention of fatty acids and phenolic compounds from Colombian cashew (Anacardium occidentale) nut shells using pyrolysis: towards a sustainable biodiesel production. Heliyon 2023;9:e18632. 8.
[18] Castro MCMD. Preparación de carbones activados con KOH a partir de residuo de petróleo: adsorción de hidrógeno. 2013.
[19] Dziejarski B, Faust R, Serafin J, Krzyżyńska R, Andersson K, Knutsson P. Insights into activation pathways of recovered Carbon Black (rCB) from End-of-Life Tires (ELTs) by potassium-containing agents. ACS Omega 2024;9(29):31814–31.
[20] Serafin J, Dziejarski B, Rodríguez-Estupiñán P, Fernández VB, Giraldo L, Sreńscek-Nazzal J, Moreno-Piraján JC. Effective synthesis route of renewable activated biocarbons adsorbent for high CO2, CH4, H2, N2, C2H4 gas storage and CO2/N2, CO2/CH4, CO2/H2, C2H4/CH4 selectivity. Fuel 2024;374:132462.
[21] Langmuir I. The adsorption of gases on plane surfaces of glass, mica and platinum. J Am Chem Soc 1918;40(9):1361–403.
[22] Freundlich HMF. Over the adsorption in solution. J Phys Chem 1906;57(385471): 1100–7.
[23] Redlich OJDL, Peterson DL. A useful adsorption isotherm. J Phys Chem 1959;63 (6):1024. 1024.
[24] Toth J. State equation of the solid-gas interface layers. Acta Chim Hung 1971;69: 311–28.
[25] Sips R. Combined form of Langmuir and Freundlich equations. J Chem Phys 1948; 16(429):490–5.
[26] Temkin MI. Kinetics of ammonia synthesis on promoted iron catalysts. Acta Physiochim. URSS 1940;12:327–56.
[27] Gong J, Liu R, Sun Y, Xu J, Liang M, Sun Y, Long L. Preparation of high-performance nitrogen doped porous carbon from cork biomass by K2CO3 activation for adsorption of rhodamine B. Ind Crop Prod 2024;208:117846.
[28] McCusker LB, Liebau F, Engelhardt G. Nomenclature of structural and compositional characteristics of ordered microporous and mesoporous materials with inorganic hosts (IUPAC Recommendations 2001). Pure Appl Chem 2001;73 (2):381–94.

[29] Serafin J, Narkiewicz U, Morawski AW, Wróbel RJ, Michalkiewicz B. Highly microporous activated carbons from biomass for CO2 capture and effective micropores at different conditions. J CO2 Util 2017;18:73–9.

[30] Fu J, Zhang J, Jin C, Wang Z, Wang T, Cheng X, Ma C. Effects of temperature, oxygen and steam on pore structure characteristics of coconut husk activated carbon powders prepared by one-step rapid pyrolysis activation process. Bioresour Technol 2020;310:123413.

[31] Leng L, Xiong Q, Yang L, Li H, Zhou Y, Zhang W, Huang H. An overview on engineering the surface area and porosity of biochar. ScI Total Environ 2021;763: 144204.

[32] Serafin J, Dziejarski B, Junior OFC, Sreńscek-Nazzal J. Design of highly microporous activated carbons based on walnut shell biomass for H2 and CO2 storage. Carbon 2023;201:633–47.

[33] Pedicini R, Maisano S, Chiodo V, Conte G, Policicchio A, Agostino RG. Posidonia Oceanica and Wood chips activated carbon as interesting materials for hydrogen storage. Int J Hydrogen Energy 2020;45(27):14038–47.

[34] Serafin J, Román-Martínez MC, Saidi M, Gallego AR, Atlas S, Ouzzine M. Valorization of argan paste cake waste: enhanced CO2 adsorption on chemically activated carbon. J Anal Appl Pyrol 2024:106637.

[35] Maisano S, Urbani F, Mondello N, Chiodo V. Catalytic pyrolysis of Mediterranean sea plant for bio-oil production. Int J Hydrogen Energy 2017;42(46):28082–92.

[36] Spokas KA. Review of the stability of biochar in soils: predictability of O: C molar ratios. 2010.

[37] Xu, Y., Liu, Y., Zhan, W., Zhang, D., Liu, Y., Xu, Y., & Wu, Z. Enhancing Co2 capture with K2co3-activated carbon derived from peanut shell. Available at: SSRN 4688078.

[38] Hwang IJ, Vo TA, Choi SS, Kim J, Hwang HT, Kim SS. Preparation of activated carbon from ginkgo leaves by steam activation for adsorption application with isotherm and kinetics. Biomass Bioenergy 2024;182:107097.

[39] Attia YA, Ezet AE, Saeed S, Galmed AH. Nano carbon-modified air purification filters for removal and detection of particulate matters from ambient air. Sci Rep 2024;14(1):621.

[40] Xie J, Fu W, Zhang X, Song G, Wu H, Zhou M. Cobalt species immobilized on nitrogen-doped ordered mesoporous carbon for highly efficient catalytic ozonation of atrazine. Separ Purif Technol 2024;335:126077.

[41] Verma V, Gurnani L, Das A, Kumari N, Dasgupta T, Mukhopadhyay A. Reduced graphene oxides prepared via explosive and non-explosive thermal reduction: structural evolution, functional properties and reinforcing efficacy. Carbon 2023; 209:118007.

[42] Efimov MN, Muratov DG, Klyuev AL, Zhilyaeva NA, Vasilev AA, Ozkan SZ, Karpacheva GP. Ultrasonic treatment duration: a nuanced parameter in synthesis affecting structural properties and ORR performance of KOH-activated carbon. Diam Relat Mater 2024:110804.

[43] Fan Y, Wang Z, Guo X, Yang S, Jia H, Tao Z, Li J. Expanded graphite/graphene composites for high through-plane thermal conductivity. Diam Relat Mater 2024: 110865.

[44] Gholizadeh F, Izadbakhsh A, Huang J, Zi-Feng Y. Catalytic performance of cubic ordered mesoporous alumina supported nickel catalysts in dry reforming of methane. Microporous Mesoporous Mater 2021;310:110616.

[45] Chen D, Zhang W, Luo K, Song Y, Zhong Y, Liu Y, Guo X. Hard carbon for sodium storage: mechanism and optimization strategies toward commercialization. Energy Environ Sci 2021;14(4):2244–62.

[46] Pedicini R, Maisano S, Chiodo V, Conte G, Policicchio A, Agostino RG. Posidonia Oceanica and Wood chips activated carbon as interesting materials for hydrogen storage. Int J Hydrogen Energy 2020;45(27):14038–47.

[47] Mohan M, Sharma VK, Kumar EA, Gayathri V. Hydrogen storage in carbon materials—a review. Energy Storage 2019;1(2):e35.

[48] Plaza MG, Pevida C, Arias B, Casal MD, Martín CF, Fermoso J, Pis JJ. Different approaches for the development of low-cost CO 2 adsorbents. J Environ Eng 2009; 135(6):426–32.

[49] Huang CC, Chen HM, Chen CH. Hydrogen adsorption on modified activated carbon. Int J Hydrogen Energy 2010;35(7):2777–80.

[50] Doğan M, Sabaz P, Bicil Z, Kizilduman BK, Turhan Y. Activated carbon synthesis from tangerine peel and its use in hydrogen storage. J Energy Inst 2020;93(6): 2176–85.

[51] Ullah Rather S. Preparation, characterization and hydrogen storage studies of carbon nanotubes and their composites: a review. Int J Hydrogen Energy 2020;45 (7):4653–72.

[52] Nuhnen A, Janiak C. A practical guide to calculate the isosteric heat/enthalpy of adsorption via adsorption isotherms in metal–organic frameworks, MOFs. Dalton Trans 2020;49(30):10295–307.

[53] Ghosh SK, Bandyopadhyay A. Adsorption of methylene blue onto citric acid treated carbonized bamboo leaves powder: equilibrium, kinetics, thermodynamics analyses. J Mol Liq 2017;248:413–24.

[54] Serafin J, Dziejarski B, Solis C, de la Piscina PR, Homs N. Medium-pressure hydrogen storage on activated carbon derived from biomass conversion. Fuel 2024; 363:130975.

[55] Myers AL, Prausnitz JM. Thermodynamics of mixed-gas adsorption. AIChE J 1965; 11(1):121–7.

[56] Ray KG, Olmsted DL, Houndonougbo Y, Laird BB, Asta M. Origins of ch4/co2 adsorption selectivity in zeolitic imidazolate frameworks: A van der waals density functional study. J Phys Chem C 2013;117(28):14642–51.

[57] Peng X. Impact of realistic vs. slit models of activated carbon on H2 and H2S Adsorption, and H2/CO2, CH4/H2S separation. Separ Purif Technol 2024:126538.

[58] Herm ZR, Krishna R, Long JR. CO2/CH4, CH4/H2 and CO2/CH4/H2 separations at high pressures using Mg2 (dobdc). Microporous Mesoporous Mater 2012;151: 481–7.

[59] https://cptcorp.vn/current-market-situation-and-cashew-exports-in-vietnam/.